Int J Earth Sci (Geol Rundsch) (2016) 105:1507–1524
DOI 10.1007/s00531-015-1271-2

ORIGINAL PAPER

Complete Alpine reworking of the northern Menderes Massif, western Turkey

B. Cenki-Tok[1] · M. Expert[1,2] · V. Işık[3] · O. Candan[4] · P. Monié[1] · O. Bruguier[1]

Received: 2 December 2014 / Accepted: 24 October 2015 / Published online: 26 November 2015

Abstract This study focuses on the petrology, geochronology and thermochronology of metamorphic rocks within the northern Menderes Massif in western Turkey. Metasediments belonging to the cover series of the Massif record pervasive amphibolite-facies metamorphism culminating at ca. 625–670 °C and 7–9 kbars. U–Th–Pb in situ ages on monazite and allanite from these metapelites record crustal thickening and nappe stacking associated with the internal imbrication of the Anatolide–Taurides platform during the Eocene. In addition, new $^{39}Ar/^{40}Ar$ single muscovite grain analyses on deformed rocks were performed in three localities within the northern Menderes Massif and ages range from 19.8 to 25.5 Ma. These mylonites may be related to both well-known detachments, Simav to the north and Alaşehir to the south, which accommodate Oligo–Miocene exhumation of the Menderes core complex. U–Th–Pb data on monazite grains (22.2 ± 0.2 Ma) from migmatites emplaced within the Simav detachment confirm these ages.

Keywords Menderes Massif · Metamorphic core complex · U–Pb geochronology · Thermochronology · Amphibolite-facies metamorphism

✉ B. Cenki-Tok
cenkitok@gm.univ-montp2.fr

[1] Géosciences Montpellier, UMR 5243, Université de Montpellier, Place E. Bataillon, 34000 Montpellier, France

[2] Faculté des Sciences et Techniques de Nantes, 2, rue de la Houssinière, 44322 Nantes, France

[3] Jeoloji Müh, Tektonik Araştırma Grubu, Ankara Üniversitesi Mühendislik Fak, Ankara, Turkey

[4] Jeoloji Müh, Bölümü, Dokuz Eylül Üniversitesi Mühendislik Fak, Buca, İzmir, Turkey

Introduction

Deformation of the earth's lithosphere involves a complex interplay between brittle and ductile processes at various structural levels. Metamorphic core complexes are highly metamorphosed rocks exhumed from mid-crustal levels to near surface. They form during continental extension when deformation in the upper crust is localised in detachment faults, which are low angle to horizontal shear zones that juxtapose rock suites of varied lithology, age and deformation history (Whitney et al. 2013). These structures have been extensively studied using a variety of techniques, e.g. field-based studies (e.g. Miller et al. 1983; Bozkurt and Park 1994; Gautier and Brun 1994; Işık et al. 2003), numerical modelling (e.g. Buck et al. 1998; Lavier et al. 1999; Tirel et al. 2004, 2008; Rey et al. 2009a; Schenker et al. 2012) and analogue modelling (e.g. Brun and van den Driessche 1994; Malavieille 2010). Metamorphic core complexes and extensional structures are widely distributed within the Aegean Sea itself and in its vicinity from western Turkey, Greece and Bulgaria (Fig. 1a). The presence of Cordilleran-type metamorphic core complexes in the Aegean region was first proposed by Lister et al. (1984) based on their work on the Cycladic complex in the Aegean Sea and was confirmed by several studies in the 1990s (Rhodope Massif: Dinter and Royden 1993; Kazdag Massif: Okay and Satır 2000; Cycladic complex: Buick, 1991; Gautier and Brun 1994; Vandenberg and Lister 1996; Menderes Massif: Bozkurt and Park 1994; Hetzel et al. 1995; Işık and Tekeli 2001; Gessner et al. 2001a, b) (Fig. 1b).

The Menderes Massif (MM) has recorded tectono-metamorphic events that are typically Aegean. Although the metamorphic core complex origin of the MM has been generally accepted, the timing, the mechanism of extensional

events and the role of inherited pre-existing structural and thermal framework in the Massif remain poorly understood. Several detachment faults and/or related shear zones that controlled the exhumation of the MM have been described and mapped (e.g. Işık et al. 2003, 2004). The exhumation history of the MM has been discussed in the literature by several authors (e.g. Ring et al. 2003; Seyitoglu et al. 2004; ten Veen et al. 2009; van Hinsbergen 2010), but information concerning the Alpine tectono-metamorphic evolution of the MM is lacking. According to Ring et al. (2003), the MM was exhumed symmetrically along the south-dipping Lycian detachment and north-dipping Simav detachment. On the contrary, according to Seyitoglu et al. (2004) the Massif exhumed asymmetrically along the north-dipping Datça-Kale main breakaway fault and its northern continuation, the Simav detachment during the Oligocene. Later stage of the exhumation was characterised along the bivergent Alasehir and Büyük Menderes detachment faults (Ring et al. 2003; Seyitoglu et al. 2004).

The aim of this study is to understand better Alpine metamorphism and exhumation processes of the northern Menderes Massif (NMM). We report the widespread occurrence of Eocene Barrovian-type metamorphism in cover series as well as the presence of mylonites Oligo–Miocene in age that we tentatively link to the Simav and Alaşehir detachment systems. The approach followed in this study includes: (1) the characterisation of metamorphic conditions through petrographic observations and thermodynamic modelling and (2) the dating with U–Pb geochronological and Ar–Ar thermochronological methods of both high-temperature (HT) and low-temperature (LT) thermal and deformational events.

Geological setting

The MM derives from a continental block of Gondwanian origin (the Anatolide–Tauride Block; Kröner and Sengör 1990; Hetzel and Reischmann 1996; Gessner et al. 2004). As a consequence of the closure of the northern branch of the Neotethys (Okay 2001; Okay et al. 2008; Candan et al. 2005; Bozkurt et al. 2008; Torsvik and Cocks 2009) or eastward continuity of the Pindos Ocean in western Anatolia (Pourteau et al. 2013), the Anatolide–Taurides platform underwent Eocene subduction and subsequent collision causing Alpine metamorphism. Today the suture zone (İzmir–Ankara–Erzincan suture zone) separates the Sakarya zone to the N and the Anatolide–Tauride platform (Anatolides and Taurides) to the S (Fig. 1b). Anatolides are assumed to be the metamorphic equivalents of the Taurides (Okay 2001; Candan et al. 2005) and are characterised by the early Alpine convergence history represented by the well-preserved HP/LT (high-pressure/low-temperature) Alpine metamorphism. A continuous younging of HP/LT metamorphism related to northward subduction and internal imbrications of the Anatolide–Tauride platform is presently assumed (Candan et al. 2005; Pourteau et al. 2013). From north to south, the convergence involved several HP/LT metamorphic units representing the existence of subduction(s) in western Turkey in a time range between ca. 90 and 45 Ma: the Tavsanli zone (80 ± 5 Ma; Campanian, Sherlock et al. 1999), the Ören–Afyon unit (between 70 and 65 Ma; Maastrichtian, Pourteau et al. 2013) and the Menderes Massif (Kurudere–Nebiler unit; between 52 and 45 Ma, middle Eocene; Pourteau et al. 2013).

The MM is traditionally divided into northern, central and southern submassifs based on the presence of the E–W-trending Alaşehir (Gediz) and Büyük Menderes grabens (Işık et al. 2004). The central MM (Aydın and Bozdağ mountains) is separated from the northern Massif, which is also termed as Demirci–Gördes submassif) by the Alaşehir graben with the Alaşehir detachment fault (or Kuzey detachment) to the north, and from the southern Massif (known also as Çine submassif) by the Büyük Menderes (BM) graben with the BM detachment fault to the south (e.g. Işık et al. 2003) (Fig. 1b, c). The whole massif is composed of a series of crystalline rock units with a complex Alpine and Pan-African metamorphic, igneous and structural history (Bozkurt et al. 1993; Bozkurt and Park 1994; Satir and Friedrichsen 1986; Hetzel and Reischmann 1996; Loos and Reischmann 1999; Bozkurt and Oberhänsli 2001; Ring et al. 2003; Gessner et al. 2001a, b, 2004; Oberhänsli et al. 1997, 2010; Candan et al. 2001, 2011, Koralay et al. 2012).

The key features of this extensional metamorphic complex are presented in van Hinsbergen (2010) and references therein. In the southern MM, the Kayabükü (Işık et al. 2004) (or Selimiye) shear zone (Régnier et al. 2003) is a ductile feature that contains asymmetrical structures indicating a top-to-the-south sense of shearing (Bozkurt and Park 1994). Although Bozkurt and Park (1994) and Hetzel and Reischmann (1996) suggest that this southward shearing occurred along an extensional shear zone, it may also be interpreted as a thrust-related shear zone (Collins and Robertson 1998, Ring et al. 1999, Gessner et al. 2001a, b).

The exhumation of the central MM is accommodated by two ductile-to-brittle extensional detachments along its northern (Alaşehir detachment; Isik et al. 2003) and southern margins (Büyük Menderes detachment). Those detachments are associated with supra-detachment basin sediments with early middle Miocene ages (14.5–16.5 Ma; Sen and Seyitoğlu 2009). Recent studies along the Alasehir detachment indicate that turtleback structures have been evaluated as part of a regional detachment surface (Seyitoglu et al. 2014). Syn-kinematic granite intrusions show crystallisation ages at 16–13 Ma (Catlos and Çemen 2005;

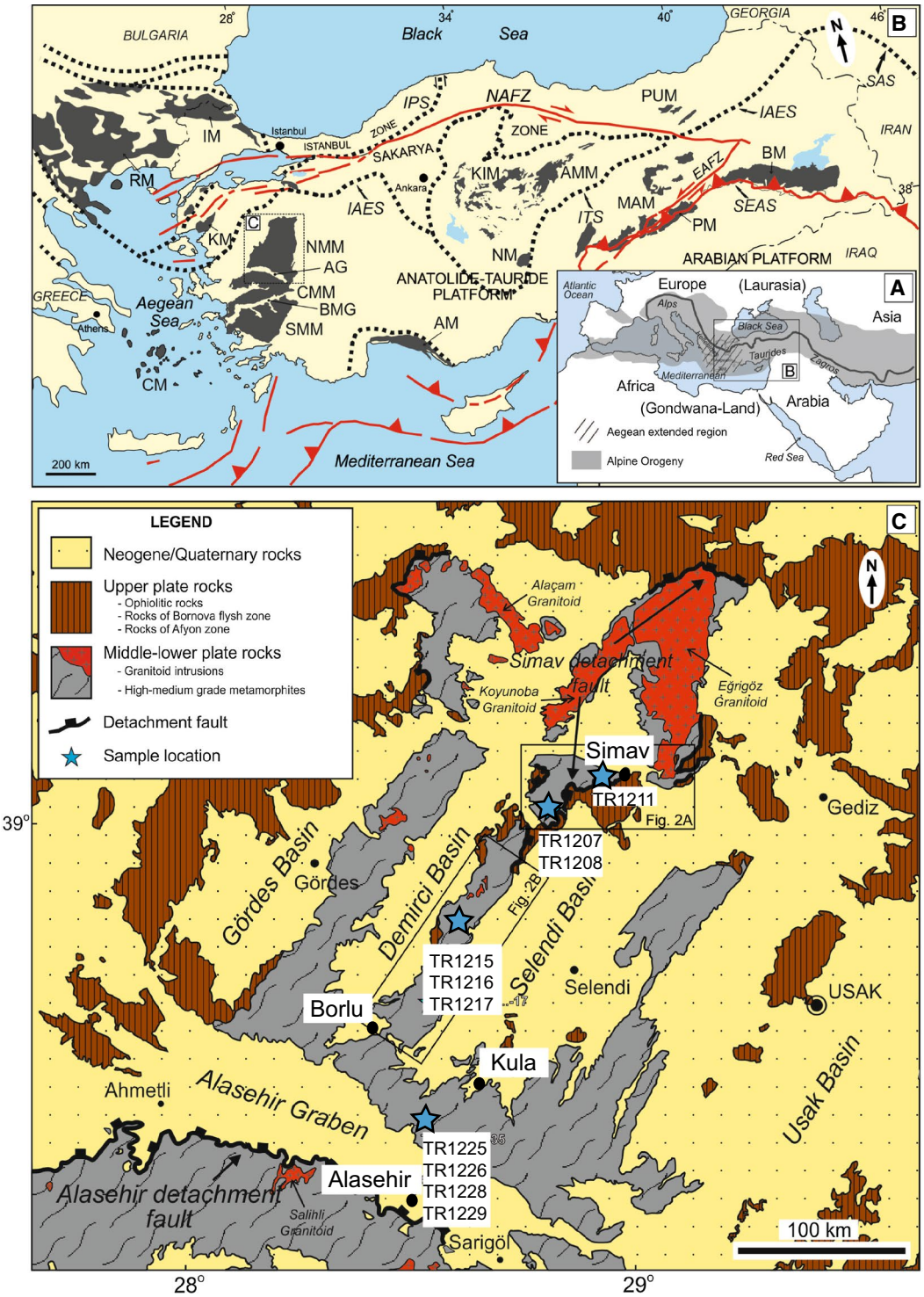

Fig. 1 **a** *Inset* map shows spatial distributions of Alpine orogeny and location of the Aegean extended region (modified after Isik et al. 2014). **b** General tectonic setting of Turkey and its near surroundings shows major faults, suture zones, continental crust domains, as well as the massifs (modified after Isik et al. 2014). **c** Simplified geological map of the northern Menderes Massif indicating sampling localities and main towns cited in the text (modified after Isik et al. 2003). The location of Fig. 2a, b is outlined by *black rectangles*. *AL* Alasehir Graben, *AM* Alanya Metamorphites, *AMM* Akdagmadeni Massif, *BM* Bitlis Massf, *BMG* Buyuk Menderes Graben, *CM* Cycladic Massif, *CMM* Central Menderes Massif, *DB* Demirci Basin, *GB* Gordes Basin, *IM* Istranja Massif, *IAEZ* Izmir–Ankara–Erzincan suture, *IPS* Intra-Pontide suture, *ITS* Intra-Tauride suture, *KM* Kazdag Massif, *KIM* Kirsehir Massif, *MM* Menderes Massif, *MAM* Malatya Metamorphites, *NM* Nigde Massif, *NMM* Northern Menderes Massif, *PM* Poturge Metamorphites, *PUM* Pulur Massif, *RM* Rhodope massif, *SAS* Seven-Akera suture, *SB* Selendi Basin, *SEAS* South-eastern Anatolian suture, *SMM* Southern Menderes Massif, *UB* Usak Basin

Glodny and Hetzel 2007; Catlos et al. 2010). In the northern and southern MM, apatite and zircon fission-track ages indicate cooling below ca. 120–60 °C between late Oligocene (ca. 27 Ma) and early Miocene (ca. 16 Ma; Ring et al. 2003). Extension is accommodated by the ductile-to-brittle Simav detachment in the northern MM (Işık and Tekeli 2001).

The Simav detachment fault (SDF; Işık and Tekeli 2001; Işık et al. 2003, 2004) bounds the MM to the N and is considered to accommodate most of its exhumation (Işık et al. 2004). It is associated with Alpine migmatites (Bozkurt and Oberhänsli 2001). The hanging wall of the SDF belongs to the Afyon zone (Pourteau et al. 2009). The role of the Alaşehir and Simav detachment faults on the Oligo–Miocene exhumation history of the MM has been suggested by Işık et al. (2003).

Sampling

Our study focuses on three localities of the NMM where we investigate relationships between mylonites and surrounding rocks (Fig. 1c). In the Simav area, we have sampled biotite–quartz–feldspar migmatites (Fig. 2a) that occur along the mountain road leading to Simav Tepe (sample TR1211; coordinates UTM/Europian59: 35 S 0666925/4327931). Based on the existence of highly retrogressed eclogites in the migmatites (Candan et al. 2001) and the Cambrian age of these eclogites (ca. 535 Ma; Oberhansli et al. 2010), a probably late Neoproterozoic age for the deposition of the protoliths of the migmatites can be envisaged. Furthermore, we sampled a garnet–kyanite–staurolite micaschist, most probably Permo-Carboniferous in age, 20 metres below the Simav detachment close to Kargınışıklar village (samples TR1207/TR1208; 35 S 0659245/4320566; Fig. 2a). In the Borlu area (Fig. 2b modified after Candan and Dora 1993), ca. 3 km west of Üsümüs village, we have sampled mylonites (sample TR1215; 35 S 0636672/4301011) as well as high-grade rocks composed of centimetre-sized garnet–kyanite–staurolite micaschist belonging to late Neoproterozoic core series of the MM (sample TR1216; 35 S 0637833/4301148). We have also sampled a low-grade chlorite schist of the upper unit a few kilometres further along the road to Borlu (sample TR1217; 35 S 0641658/4300155). In the Kula area, where we have found a typical Mesozoic–Palaeozoic cross section (Fig. 2c), we have sampled garnet–kyanite–staurolite micaschists within the Permo-Carboniferous section of the cover series of the MM (sample TR1225/TR1226-35 S 0630624/4260950) as well as high-strain metaconglomerates (sample TR1228-35 S 0630867/4262200) and black phyllites (sample TR1229) at the base of the Mesozoic sequence of the cover series.

Methods

Mineral compositions were determined with a Cameca SX100 electron probe at the University of Montpellier, operating at 20 kV accelerating voltage and 15 nA beam current. Representative mineral analyses are given in Table 1. Rock-specific equilibrium assemblage diagrams were calculated in the simplified model system Na_2O–CaO–K_2O–FeO–MgO–Al_2O_3–SiO_2–H_2O (NCKFMASH) with the free-energy minimisation programmes Theriak and Domino (de Capitani and Petrakakis 2010). More details about these softwares are available under: http://titan.minpet.unibas.ch/minpet/theriak/theruser.html. The database of Holland and Powell (1998; thermodynamic database of THERMOCALC, version 3.21) was used including recent updates (Holland and Powell 1998; Baldwin et al. 2005; Kelsey et al. 2005; White et al. 2007). Solution models for feldspars are taken from Baldwin et al.(2005), ilmenite, garnet, biotite, spinel and liquid are from White et al. (2007), orthopyroxene is from White et al. (2002), white micas is from Coggon and Holland (2002), amphibole is from Diener et al. (2007), and cordierite is from Holland et Powell (1998). Bulk rock compositions are given in Table 2. The amount of water used in the *P*–*T* diagram calculations was estimated from a T-M(H_2O) pseudosection so that the assemblage is just water-saturated below the solidus and that free water disappears within 10–20 °C once the solidus is reached (White et al. 2002). Abbreviations used in the text and figures follow Whitney and Evans (2010) except for white mica (Wm).

Fresh samples were selected for step-heating laser probe $^{40}Ar/^{39}Ar$ dating. These samples were crushed and sieved, and single grains of micas about 0.5–0.7 mm in diameter were handpicked under binocular microscope and ultrasonically cleaned in acetone and distilled water. Micas were packaged in aluminium foils and irradiated in the core of the Triga Mark II nuclear reactor of Pavia (Italia) with several aliquots of the Fisch Canyon sanidine standard (28.03 ± 0.08 Ma, Jourdan and Renne (2007) as flux monitor. Argon isotopic interferences on K and Ca were determined by irradiation of KF and CaF_2 pure salts from which the following correction factors were obtained: $(^{40}Ar/^{39}Ar)_k$ = 0.00969 ± 0.00038, $(^{38}Ar/^{39}Ar)_k$ = 0.01297 ± 0.00045, $(^{39}Ar/^{37}Ar)_{Ca}$ = 0.0007474 ± 0.000021 and $(^{36}Ar/^{37}Ar)_{Ca}$ = 0.000288 ± 0.000016. Argon analyses were performed at Géosciences Montpellier (France) with an analytical system that consists of: (a) an IR-CO_2 laser of 100 kHz used at 5–15 % during 60 s; (b) a lenses system for beam focusing; (c) a steel chamber with a drilled copper plate; (d) an inlet line for purification of gases including two Zr–Al getters; and (e) a multi-collector mass spectrometer (Argus VI from Thermo Fisher). A self-made software is used to control the

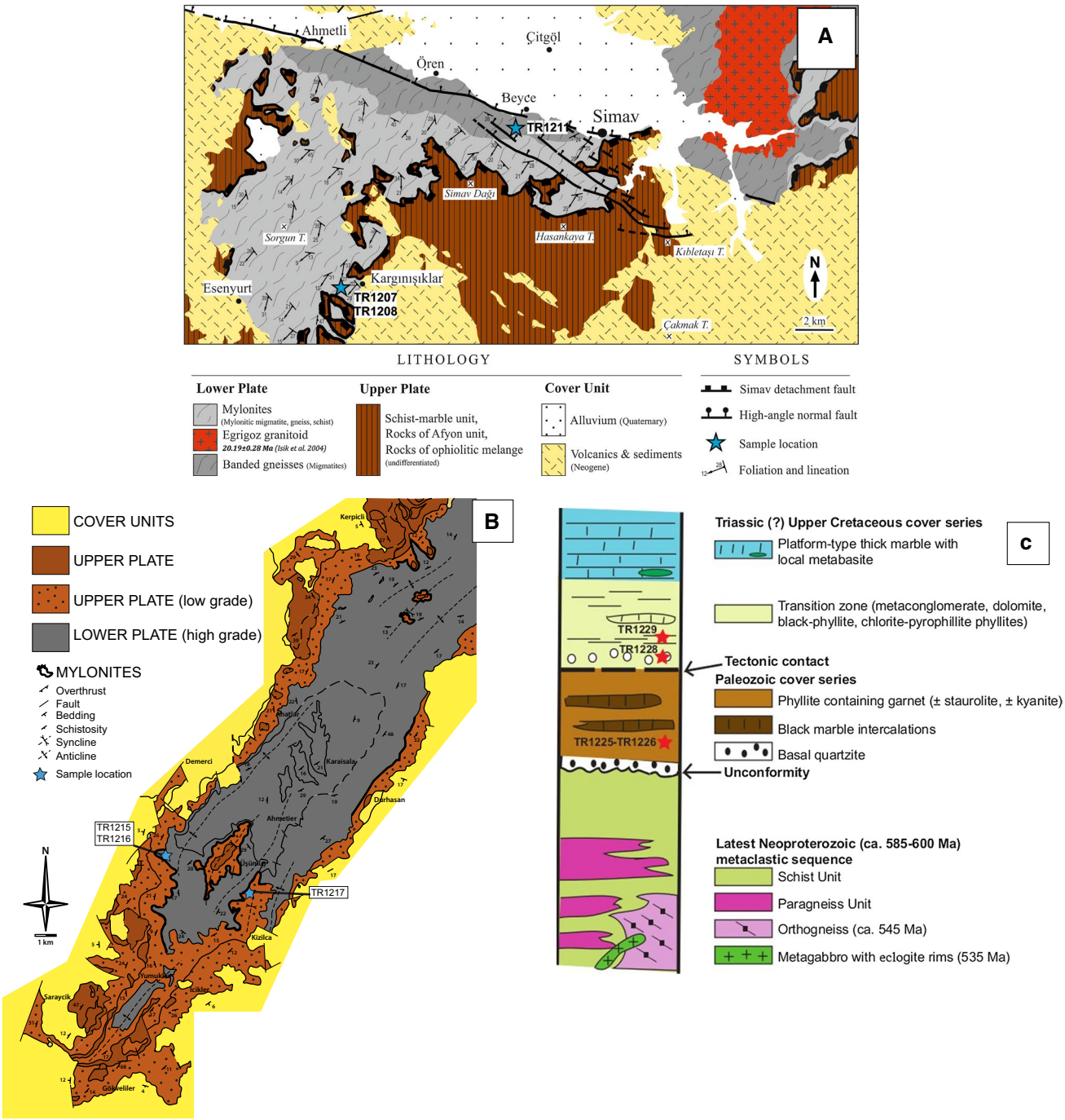

Fig. 2 **a** Geology of the Simav area (modified from Isik and Tekeli (2001), Isik et al. 2004). **b** Geological map of the Borlu area (modified after Candan and Dora 1993). **c** Schematic stratigraphic section of the Kula area. *Stars* indicate sampling locations

laser intensity, the timing of extraction/purification and the data acquisition. A blank analysis was done every three analyses to evaluate the argon background within the whole analytical system. The ArArCalc software© v2.5.2 was used for data reduction and plotting. The two-sigma errors reported on plateau, isochron and total gas ages include the error on the irradiation factor J. Atmospheric ^{40}Ar was estimated using a value of the initial ^{40}Ar/^{36}Ar of 295.5. Results are summarised in Table 3, and a complete set of isotopic data are given in the Appendix.

U–Pb dating of allanite and monazite was performed in situ on ca. 100-µm-thick sections analysed using a Thermo Finnigan Element XR sector field ICPMS (Thermo Fisher Scientific, Germany and USA) coupled to a GeoLas Q + CompEx-102 193-nm ArF excimer laser ablation system (Lambda Physik, Germany) at the University

Table 1 Representative EMPA analyses of major minerals

Garnet				Staurolite				Plagioclase			Biotite				Muscovite			
Sample	TR1207	TR1216	TR1225	Sample	TR1207	TR1216	TR1225	Sample	TR1216	TR1217	Sample	TR1207	TR1216	TR1225	Sample	TR 1207	TR 1217	TR 1228
SiO_2	37.29	38.38	37.95	SiO_2	27.67	28.14	28.06	SiO_2	66.33	63.74	SiO_2	35.62	37.18	36.07	SiO_2	46.40	46.77	46.48
Al_2O_3	21.86	22.03	21.95	Al_2O_3	54.04	55.25	54.81	Al_2O_3	21.93	23.08	Al_2O_3	21.66	19.33	17.91	Al_2O_3	36.64	33.69	34.59
TiO_2	0.01	0.00	0.05	TiO_2	0.75	0.66	0.61	TiO_2	0.00	0.03	TiO_2	0.73	1.47	1.67	TiO_2	0.86	0.94	0.28
FeO	36.68	33.82	32.98	FeO	12.96	12.72	12.76	FeO	0.00	0.05	FeO	21.17	14.91	16.23	FeO	1.07	2.90	2.93
MgO	3.18	6.00	3.58	MgO	1.73	2.15	1.18	MgO	0.00	0.00	MgO	7.56	13.25	12.18	MgO	0.64	1.13	0.99
MnO	0.84	0.85	0.03	MnO	0.05	0.12	0.03	MnO	0.01	0.00	MnO	0.06	0.02	0.00	MnO	0.01	0.02	0.00
CaO	1.64	0.63	5.17	CaO	0.01	0.01	0.01	CaO	1.87	3.71	CaO	0.04	0.05	0.42	CaO	0.00	0.01	0.00
Na_2O	0.01	0.01	0.04	Na_2O	0.00	0.02	0.00	Na_2O	10.42	9.31	Na_2O	0.11	0.54	0.22	Na_2O	0.66	0.51	0.86
K_2O	0.00	0.00	0.01	K_2O	0.00	0.00	0.00	K_2O	0.10	0.23	K_2O	8.48	8.59	7.37	K_2O	9.89	10.00	9.09
Total	101.50	101.71	101.77	Total	97.20	99.09	97.47	Total	100.67	100.14	Total	95.43	95.35	92.06	Total	96.17	95.95	95.23
Cations (normalised to 12 oxygens)				Cations (normalised to 48 oxygens)				Cations (normalised to 8 oxygens)			Cations (normalised to 12 oxygens)				Cations (normalised to 12 oxygens)			
Si	2.96	2.98	2.98	Si	7.86	7.83	7.93	Si	2.89	2.81	Si	2.70	2.74	2.77	Si	3.04	3.11	3.10
Al	2.05	2.02	2.02	Al	18.09	18.12	18.25	Al	1.13	1.20	Al	1.93	1.68	1.62	Al	2.83	2.64	2.72
Ti	0.00	0.00	0.00	Ti	0.16	0.14	0.13	Ti	0.00	0.00	Ti	0.04	0.08	0.10	Ti	0.04	0.05	0.01
Fe	2.44	2.20	2.20	Fe	3.08	2.96	3.01	Fe	0.00	0.00	Fe	1.34	0.92	1.04	Fe	0.06	0.16	0.16
Mg	0.38	0.70	0.70	Mg	0.73	0.89	0.50	Mg	0.00	0.00	Mg	0.85	1.46	1.39	Mg	0.06	0.11	0.10
Mn	0.06	0.06	0.06	Mn	0.01	0.03	0.01	Mn	0.00	0.00	Mn	0.00	0.00	0.00	Mn	0.00	0.00	0.00
Ca	0.14	0.05	0.05	Ca	0.00	0.00	0.00	Ca	0.09	0.18	Ca	0.00	0.00	0.03	Ca	0.00	0.00	0.00
Na	0.00	0.00	0.00	Na	0.00	0.01	0.00	Na	0.88	0.80	Na	0.02	0.08	0.03	Na	0.06	0.07	0.11
K	0.00	0.00	0.00	K	0.00	0.00	0.00	K	0.01	0.01	K	0.82	0.81	0.72	K	0.83	0.85	0.77
X Prp	0.13	0.23	0.14	X Mg	0.19	0.23	0.14	% An	0.09	0.18	X Mg	0.39	0.61	0.57	X Mg	0.52	0.41	0.38
X Alm	0.81	0.73	0.72					% Ab	0.91	0.82								
X Grs	0.05	0.02	0.14															
X Sps	0.02	0.02	0.00															

XMg = Mg/(Mg + Fe) for staurolite, biotite and muscovite

For garnet, X Prp is Mg(Mg + Fe + Ca + Mn), X Alm is Fe(Mg + Fe + Ca + Mn), X Grs is Ca(Mg + Fe + Ca + Mn), X Sps is Mn(Mg + Fe + Ca + Mn)

Table 2 Bulk rock compositions used for thermodynamic modelling

	TR 1207	TR 1216	TR 1217	TR 1225
SiO_2 %	74.4	66.1	68.1	58.1
Al_2O_3 %	12.3	16.2	14.9	21.4
Fe_2O_3 tot %	5.2	5.9	4.7	9.6
MgO %	1.0	3.4	2.0	1.5
CaO %	0.6	0.8	1.4	1.7
Na_2O %	1.5	3.5	2.9	1.3
K_2O %	2.1	1.9	3.1	2.1
TiO_2 %	0.8	0.8	0.7	1.3
MnO %	0.1	0.0	0.0	0.1
P_2O_5 %	0.1	0.3	0.3	0.1
Ba %	0.0	0.0	0.1	0.0
Sr %	0.0	0.0	0.0	0.0
PF (110 °C)	0.1	0.1	0.1	0.1
PF (1000 °C)	1.3	1.0	1.3	2.2
Total %	99.6	100.0	99.7	99.7

of Montpellier (Géosciences Montpellier, AETE regional facility).

For monazite, analyses were performed in the static mode using a spot size of 15 μm for sample TR1211 and 5 μm for sample TR1207, a repetition rate of 3 Hz and an energy density of 10 J/cm^2 (see Bruguier et al. 2009 for more details). The monazite standard Manangotry (Poitrasson et al. 2000) was used to calibrate the 206Pb/238U ratios measured on the unknowns.

For allanite, analytical protocols and instrumental conditions followed those described in detail by Darling et al. (2012). Key points of the methodology are: (a) 40-μm-long line-raster ablation, in order to minimise time-dependent elemental fractionation and (b) external calibration of the 206Pb/238U ratios using the zircon standard G91500 (Wiedenbeck et al. 2004). The laser was generally operated at a repetition rate of 6 Hz using a beam diameter of 26 μm and an energy density of 10 J/cm^2. Because we used a non-matrix-matching standard for allanite, accuracy of the results was monitored by several analyses of a secondary reference material BONA (Gregory et al. 2007). In the course of this study, analyses of the BONA reference material yielded a TW regression age of 39.9 ± 5.3 Ma, which is within uncertainties of reference values (see Darling et al. 2012). Common lead uncorrected $^{206}Pb/^{238}U$ ages and $^{207}Pb/^{206}Pb$ ratios obtained for the BONA allanite standard over the past 2 years are 31.056 ± 1.1 % and 0.691 ± 1.3 % ($n = 32$), respectively.

For monazite and allanite, each analysis was preceded by a pre-ablation of the surface using a beam diameter of 50 μm. He was used as a cell gas to enhance sensitivity and reduce inter-elemental fractionation (Gunther and Heinrich 1999). The ThO^+/Th^+ ratio was optimised to be <1.0 %. The acquisition times for the background and the ablation interval amounted to about 15 and 45 s, respectively. Typical acquisition series consisted of an alternation of two analyses of the standard (Manangotry for monazite and G91500 for allanite) followed by five analyses of unknowns. Data were reduced using the Glitter software. Intervals of 30 s were selected in the signal and checked before the integration of time-resolved signals to avoid possible contamination by mineral inclusions. Analyses are given in Table 4 and reported in Tera–Wasserburg concordia diagrams (Tera and Wasserburg 1972) generated by Isoplot version 3.41 (Ludwig 2003).

Results

Structures and petrography

In the Simav area, the migmatite (TR1211) is composed of monotonous millimetre-sized layering of biotite-rich melanocratic and quartz- and feldspars-rich leucocratic bands. TR1207 is a high-strain micaschist with a granolepidoblastic texture. Mylonitic foliation shows NW-WNW strike directions and mostly gently dips to the *N*, whereas stretching lineations trend SSW and SW (Fig. 2a) Foliation is marked by matrix muscovite and biotite surrounding kyanite and garnet porphyroblasts (up to 1 mm). Garnet is usually helicitic (Fig. 3a), locally elongated and boudinaged. Locally small (<200 μm) staurolite crystals occur. Asymmetry of porphyroblasts as well as S–C' fabrics indicates top-to-the-NE sense of shear. In the Borlu area, sample TR1216 is a low-strain micaschist with centimetre-sized porphyroblasts of garnet, kyanite and staurolite (Fig. 3b). Biotite marks a weak foliation and is locally chloritised. TR1217 is a medium strained greenschist. Schistosity is marked by alternating millimetre-sized layers of quartzo-feldspathic bands and oriented micas associated

Table 3 Results for Ar/Ar age dating

Sample	Total age	Plateau age	% ^{39}Ar	Intercept age	$^{40}Ar/^{36}Ar$	MSWD
TR1208 muscovite	20.1 ± 0.2	19.9 ± 0.3	85	19.9 ± 0.3	308 ± 13	2.37
TR1211 biotite	19.3 ± 0.5	19.8 ± 0.1	62	/	/	/
TR1215a muscovite	21.8 ± 0.1	21.8 ± 0.1	95	/	/	/
TR1228 muscovite	25.5 ± 0.1	25.4 ± 0.2	84	25.9 ± 0.2	290 ± 45	5.89

Table 4 Isotopic ratios resulting from LA-ICMPS geochronology

TR1211–Monazite				
Analysis	U238/Pb206	1 σ	Pb207/Pb206	1 σ
mb_1	289.8551	1.1594	0.0524	2.5778
mb_2	286.5330	1.1461	0.0535	2.7877
mb_3	283.2861	1.1331	0.0538	3.0483
mb_4	280.8989	1.1236	0.0537	2.7213
mb_5	277.7778	1.1111	0.0563	2.7551
mb_6	288.1844	1.1527	0.0540	2.7207
mb_7	292.3977	1.1696	0.0541	2.8096
mb_8	284.9003	1.1396	0.0536	3.0054
mb_9	285.7143	1.1429	0.0518	3.1069
mb_10	280.1120	1.1204	0.0624	2.2935
mb_11	282.4859	1.1299	0.0492	2.3998
mb_12	288.1844	1.1527	0.0498	2.5507
mb_13	288.1844	1.1527	0.0513	2.4747
mb_14	284.9003	1.1396	0.0536	2.7969
mb_15	285.7143	0.8571	0.0477	2.0567
mb_16	291.5452	0.8746	0.0483	1.9681
mb_17	288.1844	0.8646	0.0487	2.0525
mb_18	281.6901	1.1268	0.0512	3.2441
mb_19	277.0083	1.1080	0.0536	3.2451
mb_20	283.2861	1.1331	0.0556	2.8983
mb_21	280.1120	1.1204	0.0541	3.0477
mb_22	282.4859	1.1299	0.0518	2.8935
mb_23	284.9003	1.1396	0.0519	2.4451
mb_24	284.0909	1.1364	0.0554	2.7271
mb_25	277.7778	1.1111	0.0545	2.8786
mb_26	280.8989	1.1236	0.0537	2.7731
mb_27	280.1120	1.1204	0.0541	2.7337
mb_28	280.1120	1.1204	0.0533	2.7017
mb_29	285.7143	1.1429	0.0508	2.7936
mb_30	280.8989	1.1236	0.0544	2.9239
mb_31	278.5515	1.1142	0.0602	2.9260
mb_32	280.8989	1.1236	0.0531	2.7480
mb_33	281.6901	1.1268	0.0540	2.6657
mb_34	284.0909	1.1364	0.0522	2.8145
mb_35	282.4859	1.1299	0.0555	3.1729
TR1207-Monazite				
Analysis	Pb207/U235	1 σ	Pb206/U238	1 σ
bc_1	0.03570	0.00196	0.00518	0.00009
bc_5	0.03640	0.00181	0.00514	0.00009
bc_6	0.03956	0.00169	0.00565	0.00009
bc_8	0.02796	0.00129	0.00428	0.00007
bc_9	0.04583	0.00165	0.00529	0.00008
ct_1	0.04521	0.01478	0.00576	0.00037
ct_2	0.01636	0.03019	0.00475	0.00056
ct_4	0.06736	0.02661	0.00597	0.00056
ct_6	0.04160	0.01886	0.00552	0.00042
ct_8	0.04334	0.01802	0.00539	0.00039

Table 4 continued

TR1207-Monazite				
Analysis	Pb207/U235	1 σ	Pb206/U238	1 σ
ct_9	0.07273	0.04013	0.00536	0.00076
ct_12	0.14924	0.05516	0.00580	0.00085
ct_15	0.03900	0.05403	0.00387	0.00092
ct_16	0.02550	0.01800	0.00572	0.00040
ct_17	0.06619	0.03269	0.00564	0.00062
ct_18	0.10714	0.06415	0.00754	0.00115
ct_19	0.05058	0.08903	0.00604	0.00151
ct_20	0.03781	0.11371	0.00507	0.00201
ct_23	0.04374	0.03118	0.00546	0.00067
ct_24	0.04512	0.03878	0.00594	0.00073
ct_25	0.07620	0.04472	0.00450	0.00091
TR1226-Allanite				
Analysis	U238/Pb206	1 σ	Pb207/Pb206	1 σ
cu_6	3.1428	0.9837	0.8266	1.0780
cu_7	2.9236	1.0116	0.8273	1.1024
cu_8	10.2585	0.9540	0.7916	1.0611
cu_9	3.1240	1.0059	0.8227	1.0977
cu_10	3.4674	1.0055	0.8330	1.1008
cu_11	2.6126	1.0111	0.8397	1.0981
cu_12	6.0416	0.9969	0.8235	1.0990
cu_14	7.9517	1.0337	0.8043	1.1463
cu_15	8.0212	0.9465	0.7918	1.0508
cu_16	9.8522	1.0049	0.7981	1.1090
cu_17	4.0800	1.0282	0.8262	1.1245
cu_18	5.0449	1.0292	0.8035	1.1288
cu_19	3.0464	0.9901	0.8179	1.0820
cu_20	5.7412	1.0104	0.8066	1.1109
bd_1	6.3048	0.8764	0.8298	1.1473
bd_2	8.1873	0.8433	0.8164	1.1183
bd_3	2.8853	0.8454	0.8363	1.1024
bd_4	13.5777	0.8011	0.7696	1.0733
bd_5	10.3423	0.7964	0.7844	1.0670
bd_6	3.2566	0.8402	0.8260	1.0895
bd_7	4.0080	0.8457	0.8218	1.0940
bd_8	3.4130	0.8430	0.8260	1.0847
bd_9	5.0738	0.8524	0.8073	1.0950

with chlorite crystals. Foliation shows NW strike direction and mostly gently dips to the *N*. Stretching lineations trend SW (Fig. 2b). Mylonitic sample TR1215 is composed of a fine-grained recrystallised and foliated matrix of quartz, feldspars and phylosilicates wrapping around millmetre-sized porphyroclasts of rounded quartz and muscovite. In the Kula area, sample TR1225 is a high-strain micaschist with garnet, kyanite and staurolite porphyroblasts (up du 0.6 mm). Mylonitic foliation shows NNW strike direction and mostly gently dips to the *N*. Stretching lineations trend SW. Garnet is often helicitic locally microboudinaged (Fig. 3c). Schistosity is marked by fine-grained muscovite and biotite and layers rich in graphitic material. Some of staurolite and kyanite porphyroblasts (Fig. 3d) display an asymmetric structure showing top-to-the-NE shearing. TR1228 is a mylonitic metaconglomerate. The texture is grano-lepidoblastic and mostly composed of quartzo-feldspathic minerals. Mylonitic foliation is defined by muscovite, elongated epidote, tourmaline and rare chlorite. Kyanite is present locally. TR1229 is a quartzite rich in organic matter. It is composed of fine-grained micas, chlorite and recrystallised quartz.

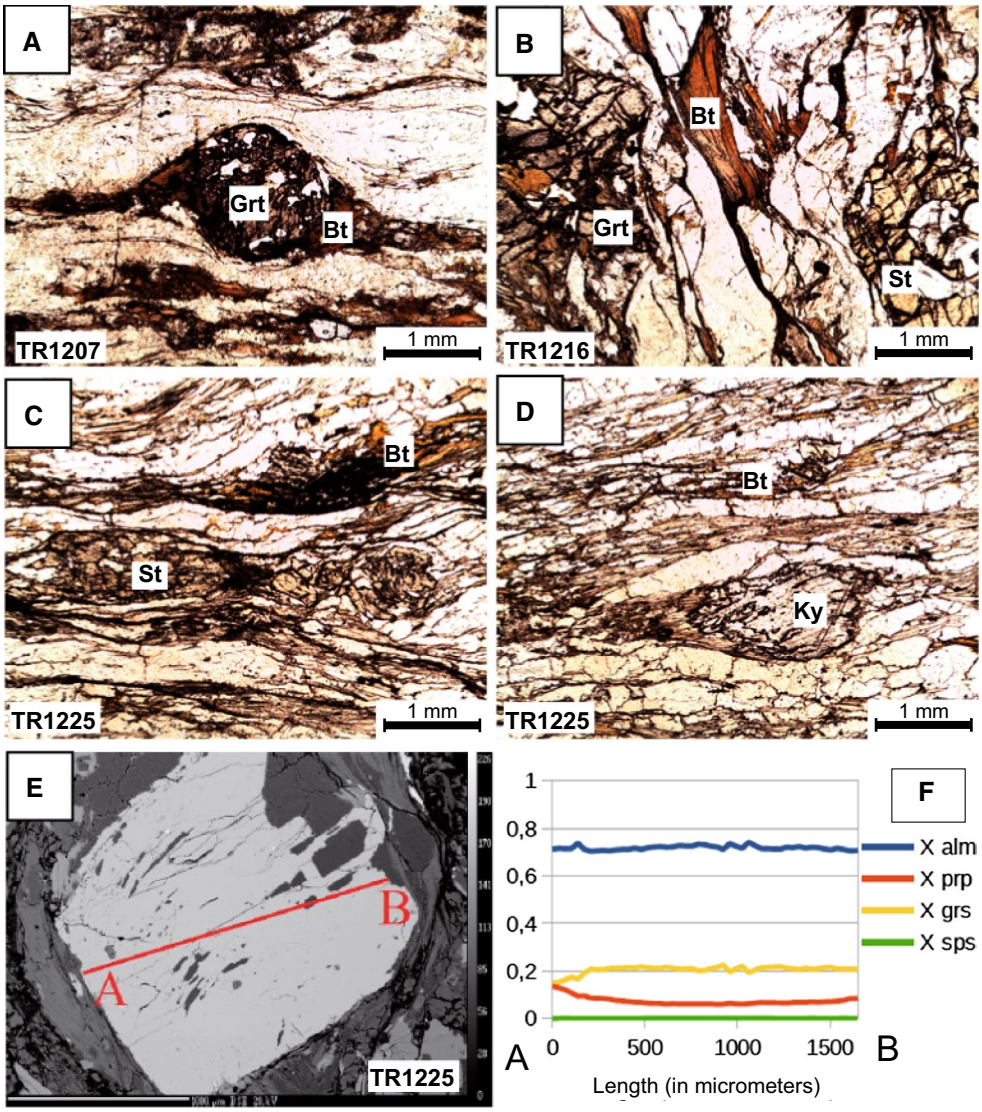

Fig. 3 Microphotographs, optical microscope plain polarised light. **a** Helicitic garnet (TR1207); **b** Garnet–staurolite–kyanite micaschist (TR1216); **c** Helicitic staurolite (TR1225); **d** Kyanite (TR1225). **e** Backscattered image of a garnet in TR1225; **f** Chemical profile through the garnet presented in E (*alm* almandine, *prp* pyrope, *grs* grossular, *sps* spessartine)

Mineral chemistry

In the following, X_{Mg} represents the ratio Mg/(Mg + Fe) for all phases except garnet (mineral abbreviations after Whitney and Evans 2010). For garnet, X_{Mg} equals Mg/(Mg + Fe + Mn + Ca), and similar definitions for X_{Fe}, X_{Mn} and X_{Ca}. Garnet chemistry (Table 1) is dominated by almandine (X_{Fe} = 0.72–0.81), followed by pyrope (X_{Mg} = 0.13–0.23), grossular (X_{Ca} = 0.02–0.14) and spessartine (X_{Mn} < 0.02). Tetrahedral alumina and the andradite component are insignificant within analytical errors. Garnet shows flat end-member profiles (Fig. 3e, f). Biotite shows vacancies in the octahedral sites that may be due to the high Ti content that may be up to 1.7 wt%. X_{Mg} is low (0.39–0.61). Analysis for muscovite shows that X_{Mg} is low (0.38–0.50) and Si (pfu) may be up to 3.10. Plagioclase has albite composition ($Ab_{80–90}$ $An_{9–18}$ $Or_{0–2}$; Table 1). Staurolite has a composition close to the ferro-staurolite end member (Table 1). Accessory minerals occurring in most of the thin sections are rutile, apatite, monazite and allanite.

Thermodynamic modelling

Results of thermodynamic modelling for the three garnet–staurolite–kyanite micaschists (TR1207, TR1216 and TR1225) as well as the greenschist (TR1217) are shown in Fig. 4. For sample TR1207 (Fig. 4a), we consider a narrow peak stability field for the assemblage garnet–kyanite–staurolite–white mica–biotite–quartz–feldspar at ca. 660 ± 5 °C and 7.7 ± 0.3 kbar. The slope of the

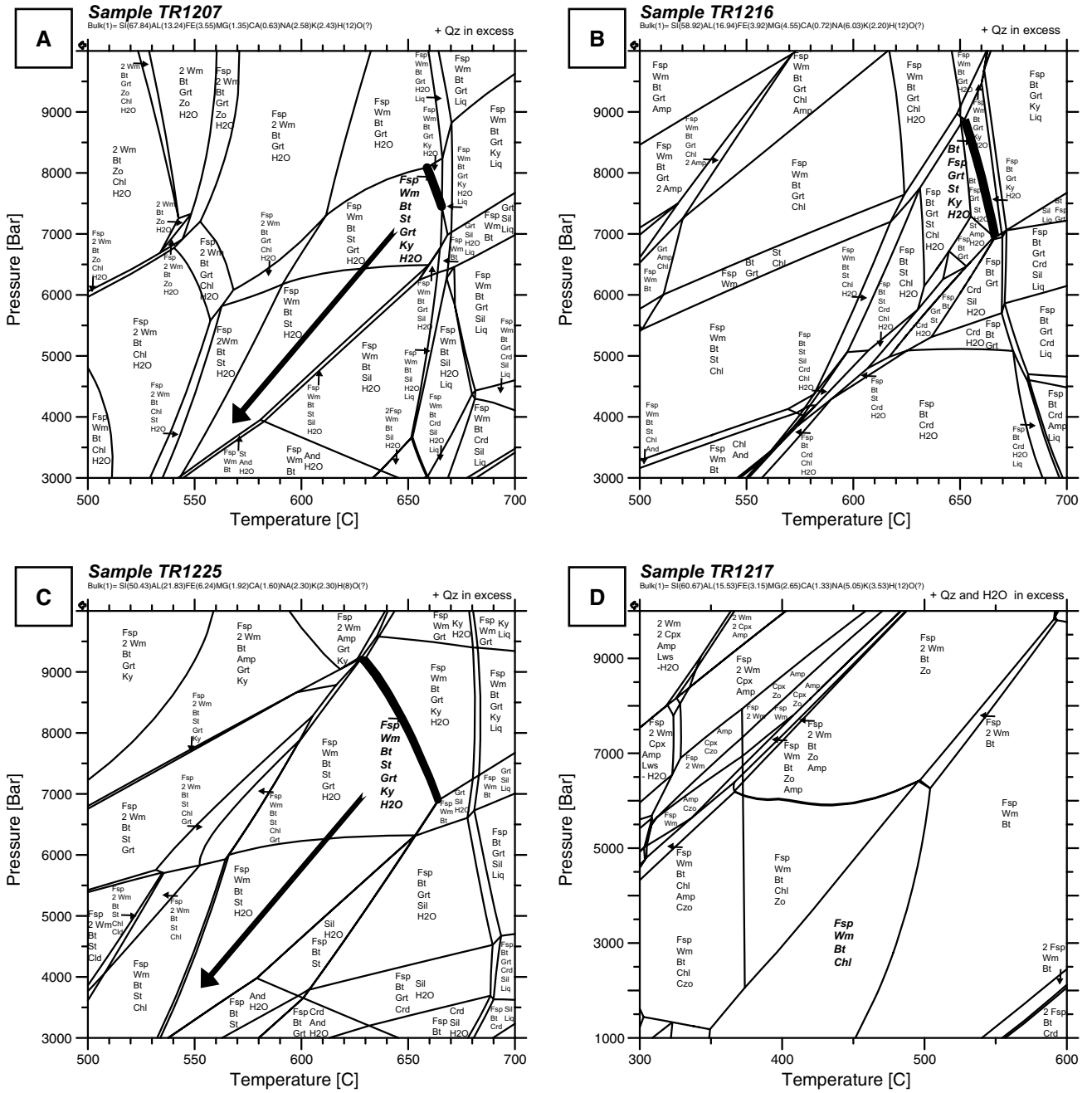

Fig. 4 Equilibrium assemblage diagrams generated by Domino-Theriak (de Capitani and Petrakakis 2010) for the four samples studied. See location in Figs. 1 and 2. Abbreviations after Whitney and Evans (2010) except for white mica (Wm)

retrograde path proposed is controlled by the fact that neither chlorite nor sillimanite appears. For sample TR1216 (Fig. 4b), peak metamorphism is in the narrow garnet–kyanite–staurolite–biotite–quartz–feldspar stability narrow field culminating at 660 ± 10 °C and 7.8 ± 1 kbar. The slope of the proposed retrograde path is in accordance with the appearance of chlorite replacing biotite locally and the absence of sillimanite, cordierite and amphibole. Equilibrium assemblage diagram for TR1225 (Fig. 4c) indicates a narrow peak stability field with the observed assemblage garnet–kyanite–staurolite–muscovite–biotite–quartz–feldspar at 645 ± 20 °C and 8 ± 1.2 kbar. The absence of cordierite, chlorite and sillimanite constrain the proposed retrograde path. Modelled peak PT conditions for these three amphibolite-facies rocks are homogeneous (625–670 °C and 7–9 kbars). The equilibrium assemblage diagram for the greenschist TR1217 (Fig. 4d) indicates a large range of stability field for the

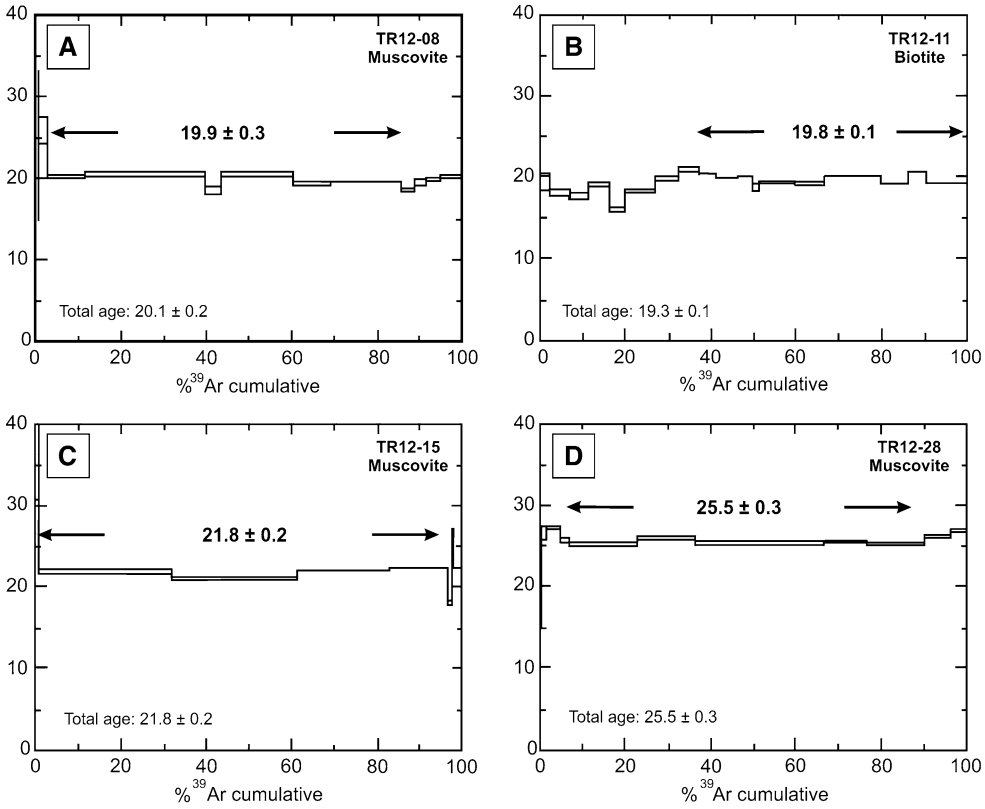

Fig. 5 Micas age spectra for the studied samples. See location in Figs. 1 and 2

biotite–chlorite–muscovite–albite–quartz observed high-variance assemblage. Maximum temperature is 500 °C, and pressure may be up to 6 kbars.

Ar–Ar thermochronology

Two samples from the Simav area were selected for Ar–Ar dating. Muscovite separated from the garnet–kyanite–staurolite schist located at the footwall of the Simav detachment (TR1208) yields a plateau age of 19.9 ± 0.3 Ma related to 85 % of ^{39}Ar released (Fig. 5a; Table 3). This is consistent with the intercept age obtained in the inverse argon correlation plot. Biotite from migmatite (TR1211) provides a similar plateau age of 19.8 ± 0.1 Ma for 62 % of ^{39}Ar released (Fig. 5b), but no intercept age can be defined in the inverse correlation plot due to the high radiogenic content of the sample. In the ultramylonite (TR1215) from the Borlu area, muscovite yields a plateau age at 21.8 ± 0.2 Ma defined by four steps that represent 95 % of the argon released (Fig. 5c). In the reverse correlation plot, the data cluster near the abscissa and no intercept has been found. Muscovite separated from the ultramylonitic metaconglomerate at the base of the Mesozoic section (TR1228) in the Kula area yields an older plateau age at 25.5 ± 0.3 Ma (Fig. 5d), in agreement with its intercept age. No evidence of excess argon is provided by the inverse correlation plot.

U–Pb geochronology on monazite and allanite

Monazite and allanite from three selected samples were dated in situ by LA-ICPMS at the University of Montpellier. Monazite grains were separated from the migmatite (TR1211) associated with the Simav detachment. These grains are small (<400 μm) and rounded, homogeneous in composition (Fig. 6a). Reported in a Tera–Wasserburg diagram (1972; Fig. 6a), data yield a lower intercept age at 22.21 ± 0.21 Ma (MSWD = 1.00, n = 35). This age is related to monazite growth and the formation of leucosome in migmatite.

Monazite grains measured in situ in thin sections from the garnet–kyanite–staurolite schists (TR1207) located at the footwall of the Simav detachment yield a lower intercept age of 33.4 ± 2.6 Ma (MSWD = 3.9; n = 21; Fig. 6b). These monazites are small (<100 μm) and rounded, mainly present as inclusions in matrix feldspars and micas. Selection of suitable analyses was made according to their Th/U ratio (between 1.9 and 8.6) presenting a reasonable amount of counts on measured isotopes. Due to the small grain size, two sessions of analyses were performed with different spot sizes (15 and 5 μm). The variability in error ellipses is a direct consequence of this choice.

Syn-kinematic allanite grains from sample TR1226, which is a garnet–kyanite–staurolite schist sampled in the Kula area, yield a lower intercept Tera–Wasserburg age at 42.3 ± 9.1 Ma (MSWD = 0.92; n = 23; Fig. 6c). Allanite

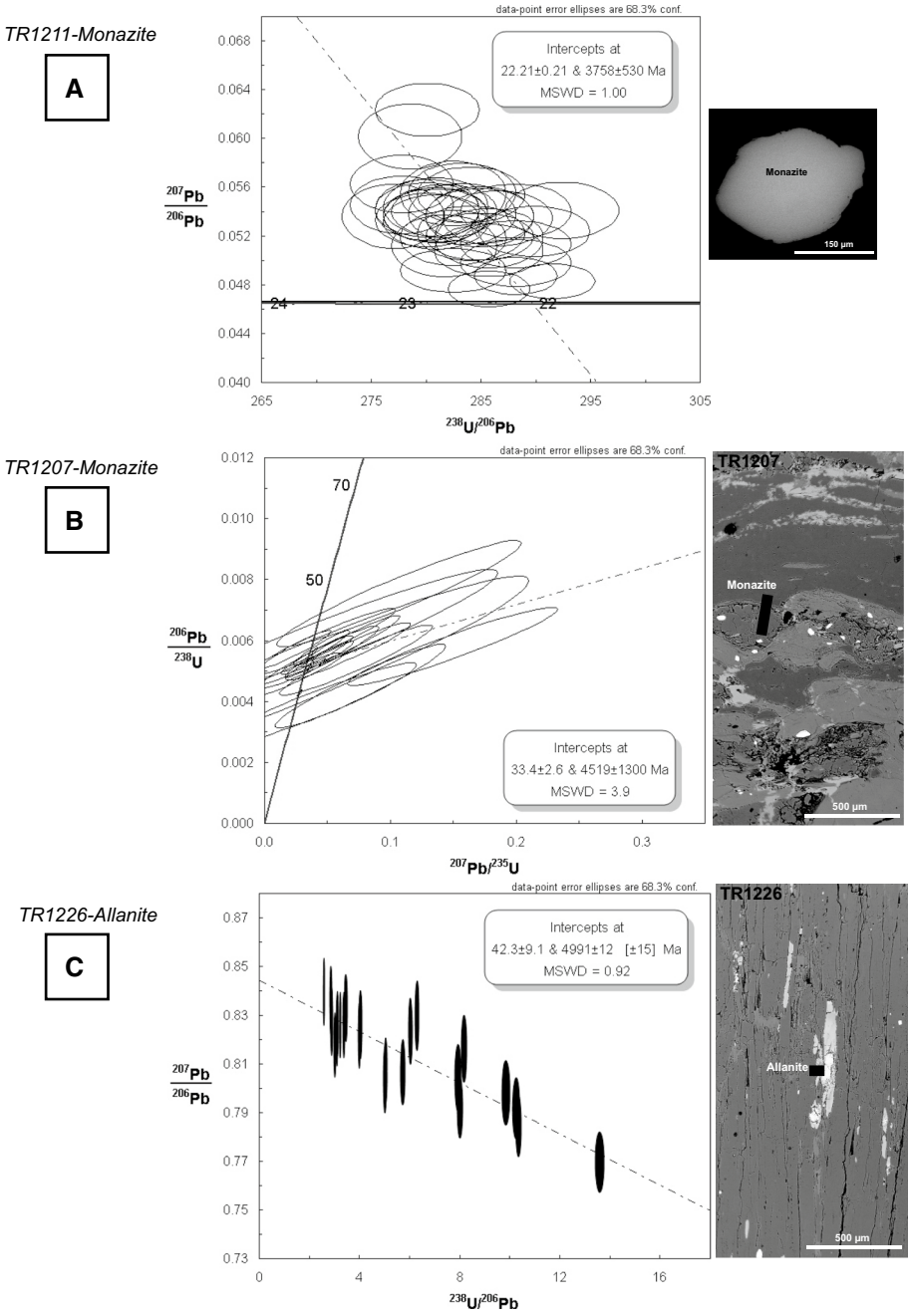

Figure 6 - Cenki-Tok et al.

Fig. 6 **a** Tera–Wasserburg diagram for monazite grains of migmatitic sample TR1211. **b** Concordia diagram for monazite grains from garnet–kyanite micaschist TR1207. **c** Tera–Wasserburg diagram for monazite grains of garnet–kyanite micaschist TR1226. See location in Figs. 1 and 2

is elongated in the foliation (Fig. 6c) and is considered syn-metamorphic as well.

Discussion

Eocene barrovian metamorphism overprint on the poly-cyclic MM basement and cover series

In this study, we report new petrological, U–Pb geochronological and Ar–Ar thermochronological data for metamorphic rocks from the NMM. Structural data are in line with previously published data (Isik and Tekeli 2001), i.e. that at least the latest component of deformation recorded within high-strain zones and mylonites indicate non-coaxial deformation and a simple shear overprint dominated by top-to-the-NNE features. Concerning metamorphism, the three studied localities point to homogeneous conditions at amphibolite-facies conditions representing common Barrovian metamorphism culminating at ca. 650 °C and 8 kbar on cover series and overprinted on poly-metamorphic basement series. Our novel age data are

useful in order to highlight regional age patterns and derive cooling rates of the terrane.

In the Simav area, ages yielded by different mineral chronometers allow us to derive long-term and short-term cooling rates. In migmatite TR1211, monazite that probably crystallises close to peak metamorphism is dated at ca. 22 Ma with U–Pb and biotite grains at ca. 20 Ma with Ar–Ar. Considering that peak temperatures during partial melting that lead to the formation of TR1211 are close to closure temperatures for U–Pb in monazite (>725 °C; Copeland et al. 1983) and taken into account a closure temperature of ca. 300 °C for Ar–Ar in biotite, we can derive a Miocene cooling rate of ca. 180 °C/Ma, associated with the main exhumation phase controlled by the Simav detachment. Similar cooling rates have been reported, for example, in the Betic orogen (Zeck et al. 1992; Monié et al. 1994) and are typical of large-scale extensional tectonics. Age data in Palaeozoic schists located at the footwall of the detachment yield a long-term cooling rate between 19 and 28 °C/Ma, with U–Pb monazite age at 33.4 ± 2.6 Ma and a muscovite Ar/Ar age of ca. 19.9 Ma. In Kula, muscovite in high-strain metaconglomerates yields an Ar/Ar age of ca. 25.5 Ma, whereas syn-kinematic and syn-metamorphic allanite in tectonically underlying Palaeozoic schists has a U–Pb age of 42.3 ± 9.1 Ma. These data yield cooling rates between 12 and 38 °C/Ma that take into account large errors on allanite age data.

A first conclusion is that crustal thickening has strongly overprinted the poly-metamorphic basement series (Candan et al. 2011; Koralay et al. 2012) and has caused the single-stage Alpine metamorphism (Barrovian type) of the cover series. This thermal event is related to an internal imbrication of the Anatolide–Tauride platform and the burial of nappe stack of the Afyon zone and Lycian nappes during southward transportation. We relate the allanite age of 42.3 ± 9.1 Ma from Kula to the near peak time of Alpine metamorphism of the MM. Therefore, we propose that this Alpine event shall be Eocene. This age is consistent with literature data. For example, Satır and Friedrichsen (1986) published white mica ages between 48 and 63 Ma with an average age of 56 ± 1 Ma and biotite ages between 27 and 50 Ma with an average age of 35 ± 5 Ma. Hetzel and Reischman (1996) published Ar–Ar ages between 43 and 37 Ma, and Bozkurt and Satir (2000) reported Rb–Sr mica ages from orthogneisses at ca. 62–43 Ma. Monazite Th–Pb ages of 47.1 ± 6.3, 44.7 ± 6.1 and 42.8 ± 3.6 Ma are also reported (Catlos and Çemen 2005). In addition, the age of the oldest unit in the metamorphic cover series of the MM is Santonian–Campanian to middle Paleocene (~60 Ma; Özer et al. 2001) and the youngest non-metamorphic sedimentary cover on the Massif is Miocene in age (Yılmaz et al. 2000). This implies that amphibolite-facies metamorphism might have started in Eocene times (ca. 50 Ma) and have lasted until Oligocene times. Even though U–Pb age data for monazite and allanite in amphibolite-facies rocks are comparable within error, monazite from Simav (basement) may be slightly younger than allanite from Kula (cover series). The appearance of monazite or allanite is controlled by (1) bulk rock composition, (2) thermodynamic stability field and (3) textural relationships (see Cenki-Tok et al. 2011 for a review). In both locality protoliths, bulk rock composition and metamorphic conditions are comparable. Allanite is often considered as a precursor for monazite (Janots et al. 2008) and may be preserved in Kula. This age difference may reflect a real different timing of crystallisation for both minerals in the two regions.

Oligo–Miocene exhumation of the MM core complex and comparison with the Kazdag Massif

The regional pattern of Ar/Ar muscovite ages indicates younging from south (25.5 Ma) to north (19.9 Ma). This diachronicity of low-temperature deformation in schists does not reflect the fact that the deformation in Simav may be a precursor for the Alaşehir detachment (Işık et al. 2003). This age scatter for LT deformation related to exhumation may be linked to (1) various degree of resetting/reworking of structures related to crustal thickening; (2) shear zones between Alasehir and Simav that may be anastomosing and imbricated; and (3) diachronous exhumation within the NMM. In addition, whereas the structural position of dated mylonites (separating the MM from the overlying Afyon units) is similar in the Simav and Kula areas (i.e. corresponds to the Simav flat lying detachment), the mylonites sampled in Borlu lay within high- and low-grade units of the MM. Metamorphism in metaconglomerates in Kula is dated at 25.5 Ma, and these stratigraphically belong to the base of the Mesozoic section (Fig. 2c). They overlay Palaeozoic schists, similar to the section observed in the Selimiye area, in which the carpholite–kyanite assemblage was discovered (Rimmelé et al. 2003; Whitney et al. 2008). This high-strain zone may be a former nappe contact (Palaeozoic/Mesozoic) reworked during exhumation, thus implying partial mineral resetting. Further field work and structural studies are needed in order to refine the structural significance and the exhumation history of subunits within the NMM.

The signification of monazite U–Pb Miocene ages from Simav may be interpreted in a specific tectonic

context. In most parts of the MM, migmatites are widespread and are attributed to the Pan-African events (ca. 550 Ma; Hetzel and Reischmann 1996; Candan et al. 2011). The northernmost edge of the MM is intruded by numerous early Miocene granites (e.g. Eğrigöz granite) which continue to crop out in the north up to Evciler. These intrusions are not restricted to the MM, and they are also present in the Sakarya and Afyon zones. The entire area shows evidence for a hot crust during early Miocene. Locally, for example in the Kazdağ massif, these granites are associated with migmatites dated at 20 Ma (Okay and Satır 2000). In addition, apatite fission tracks (Cavezza et al. 2009) indicate rapid early middle Miocene exhumation for this other core complex of western Turkey. In this context, the Miocene monazite ages and migmatisation in Simav area can be attributed to this regional heat increase in the crust due to a high geotherm. These ages may also coincide with uplift and exhumation of the northern edge of MM in Miocene times. This scenario is in line with Aegean geodynamics dominated by Miocene core complex exhumation. Compared to the Cyclades, the MM shows great exposure of the basement enabling to unravel the early Alpine tectono-metamorphic history as well as pre-extensional structural framework of the region and its role in accommodating core complex exhumation.

Conclusions

Based on petrological geochronological and thermochronological data, we highlight the complete Alpine reworking under amphibolite-facies conditions of the Menderes Massif. This thermal event occurred at Eocene times and may be linked to the internal imbrication of the Anatolide–Tauride platform associated with southward transportation of the Afyon zone and Lycian nappes. Mylonites within the northern Menderes Massif are Oligo–Miocene in age and can be related, at least locally, to the well-defined Alasehir and Simav detachments which accommodated the exhumation of the MM core complex. Nevertheless, these mylonites might rework former shear zones related to the Alpine history of the terrane, and further structural work is needed in order to unravel the role of structural and thermal inheritance on the localisation of exhumation-related deformation and post-orogenic extension.

Acknowledgments Financial support from the TERMEX/MISTRALS program as well as the French Embassy in Turkey is greatly acknowledged. We thank the support of the Microsonde Sud equipment. We would like to thank C. Dullo for editorial handling and an anonymous reviewer for constructive and helpful reviews.

Appendix

	$^{40}Ar/^{39}Ar$	$^{38}Ar/^{39}Ar$	$^{36}Ar/^{39}Ar \times 1000$	% ^{39}Ar cum	% ^{40}Ar rad	Age	Error
J = 0.004922							
TR12-08 muscovite							
1	17.088	0.077	50.397	0.17	12.8	19.31	6.92
2	6.400	0.015	14.636	0.58	32.3	28.25	3.52
3	22.516	0.018	65.817	0.88	13.6	26.96	6.16
4	8.812	0.015	19.836	2.28	33.4	25.93	1.56
5	2.920	0.014	2.075	11.58	78.7	20.28	0.25
6	2.533	0.013	0.720	39.56	91.2	20.40	0.19
7	2.593	0.014	1.657	43.13	80.7	18.50	0.34
8	2.648	0.013	1.093	60.24	87.4	20.44	0.21
9	2.407	0.014	0.691	68.87	91.1	19.37	0.15
10	2.429	0.013	0.724	85.56	90.8	19.48	0.11
11	2.475	0.013	0.123	88.80	84.9	18.56	0.27
12	2.513	0.012	1.001	91.27	87.8	19.50	0.36
13	2.554	0.012	1.033	94.85	87.7	19.77	0.29
14	2.482	0.013	0.591	100.00	92.6	20.29	0.22
				Total age: 20.08 ± 0.22			
TR12-11 biotite							
1	5.045	0.033	9.586	1.93	43.7	19.45	1.06
2	2.436	0.027	1.281	6.94	84.1	18.10	0.35
3	2.358	0.025	1.165	11.24	85.0	17.71	0.29
4	2.361	0.024	0.652	15.93	91.4	19.06	0.25
5	2.236	0.026	0.143	19.57	80.7	15.95	0.26
6	2.319	0.025	0.776	26.61	89.7	18.38	0.20
7	2.292	0.024	0.131	31.13	97.9	19.81	0.20
8	2.371	0.029	0.000	36.78	99.6	20.85	0.17
9	2.308	0.025	0.000	40.85	99.6	20.29	0.14
10	2.368	0.025	0.350	46.14	95.2	19.92	0.21
11	2.278	0.027	0.000	49.57	99.6	20.03	0.12
12	2.292	0.029	0.549	51.20	92.5	18.72	0.48
13	2.190	0.026	0.000	59.25	99.6	19.26	0.12
14	2.241	0.026	0.197	66.34	97.0	19.20	0.16
15	2.317	0.025	0.137	79.61	97.8	20.02	0.11
16	2.280	0.025	0.300	86.04	95.7	19.27	0.15
17	2.339	0.023	0.000	100.00	99.6	20.57	0.10
				Total age: 19.32 ± 0.23			
TR12-15a muscovite							
1	14.191	0.075	33.692	0.49	29.8	37.17	6.53
2	2.925	0.011	1.509	31.95	84.4	21.80	0.24
3	2.524	0.013	0.426	61.10	94.6	21.08	0.15
4	2.506	0.013	0.000	83.12	99.6	22.03	0.10
5	2.525	0.013	0.000	96.38	99.6	22.20	0.12
6	2.043	0.013	0.000	97.71	99.5	17.99	0.35
7	3.009	0.008	0.001	98.15	99.7	26.59	0.56
8	2.702	0.011	0.003	100.00	99.6	23.75	1.32
				Total age: 21.79 ± 0.28			

	$^{40}Ar/^{39}Ar$	$^{38}Ar/^{39}Ar$	$^{36}Ar/^{39}Ar \times 1000$	% ^{39}Ar cum	% ^{40}Ar rad	Age	Error
TR12-28 muscovite							
1	11.931	0.043	33.104	0.20	17.9	18.89	5.91
2	4.343	0.017	7.883	0.51	46.3	17.76	2.76
3	3.204	0.011	0.628	1.49	93.9	26.52	0.87
4	3.097	0.013	0.000	4.65	99.7	27.21	0.18
5	2.917	0.010	0.000	6.73	99.7	25.64	0.31
6	2.955	0.012	0.340	22.46	96.3	25.09	0.15
7	2.995	0.013	0.135	36.67	98.3	25.97	0.02
8	2.915	0.012	0.128	66.81	98.4	25.28	0.22
9	2.893	0.012	0.000	76.51	99.7	25.43	0.10
10	2.915	0.012	0.125	90.11	98.4	25.30	0.10
11	3.010	0.015	0.123	96.50	98.5	26.14	0.26
12	3.048	0.010	0.000	100.00	99.7	26.80	0.18
				Total age: 25.53 ± 0.35			

References

Baldwin J-A, Powell R, Brown M, Moraes R, Fuck R-A (2005) Modelling of mineral equilibria in ultrahigh-temperature metamorphic rocks from the Anapolis–Itaucu Complex, central Brazil. J Metamorph Geol 23:511–531

Bozkurt E, Oberhansli R (2001) Menderes Massif (Western Turkey): structural, metamorphic and magmatic evolution —a synthesis. Int J Earth Sci 89:679–708

Bozkurt E, Park RG (1994) Southern Menderes Massif: an incipient metamorphic core complex in Western Anatolia, Turkey. J Geol Soc Lond 151:213–216

Bozkurt E, Satir M (2000) New Rb–Sr geochronology from the southern Menderes Massif (southwestern Turkey) and its tectonic significance. Geol J 35:285–296

Bozkurt E, Park RG, Winchester JA (1993) Evidence against the core/cover interpretation of the southern sector of the Menderes Massif, west Turkey. Terra Nova 5:445–451

Bozkurt E, Winchester JA, Yiğitbaş E, Ottley CJ (2008) Proterozoic ophiolites and mafic–ultramafic complexes marginal to the Istanbul Block: an exotic terrane of Avalonian affinity in NW Turkey. Tectonophysics 461:240–251

Bruguier O, Hammor D, Bosch D, Caby R (2009) Miocene incorporation of peridotite into the Hercynian basement of the Maghrebides (Edough Massif, NE Algeria): implications for the geodynamic evolution of the Western Mediterranean. Chem Geol 261:171–183

Brun J-P, Van Den Driessche J (1994) Extensional gneiss dome and detachment fault systems: structure and kinematics. Bulletin de la Société Géologique de France 165:519–530

Buck WR, Poliakov ANB (1998) Abyssal hills formed by stretching oceanic lithosphere. Nature 392:272–275

Buick IS (1991) The late-Alpine evolution of an extensional shear zone, Naxos. Greece. J Geol Soc Lond 148:93–103

Candan O, Dora O (1993) Application of schreinemakers method to a metamorphic area located at the northern flank of the Menderes Massif (Western Turkey). Bull Geol Soc Greece XXVIII(2):169–186

Candan O, Dora OO, Oberhänsli R, Cetinkaplan M, Partzsch JH, Warkus FC, Durr S (2001) Pan-African high-pressure metamorphism in the Precambrian basement of the Menderes Massif, western Anatolia, Turkey. Int J Earth Sci 89(4):793–811

Candan O, Cetinkaplan M, Oberhänsli R, Rimmelé G, Akal C (2005) Alpine high-P/low-T metamorphism of the Afyon Zone and implications for the metamorphic evolution of Western Anatolia, Turkey. Lithos 84:102–124

Candan O, Koralay E, Akal C, Kaya O, Oberhansli R, Dora OÖ, Konak N, Chen F (2011) Supra-Pan-African unconformity between core and cover series of the Menderes Massif/Turkey and its geological implications. Precambr Res 184:1–23

Catlos EJ, Cemen I (2005) Monazite ages and the evolution of the Menderes Massif, western Turkey. Int J Earth Sci 94:204–217

Catlos EJ, Baker C, Sorensen SS, Çemen Đ, Hancer M (2010) Geochemistry, geochronology, and cathodoluminescence imagery of the Salihli and Turgutlu granites (central Menderes Massif, western Turkey): implications for Aegean tectonics. Tectonophysics. doi:10.1016/j.tecto.2009.06.001

Cavezza W, Okay ZI, Zattin M (2009) Rapid early-middle Miocene exhumation of the Kazdag Massif (western Anatolia). Int J Earth Sci 98:1935–1947

Cenki-Tok B, Oliot E, Rubatto D, Berger A, Engi M, Janots E, Thomsen TB, Manzotti P, Regis D, Spandler C, Robyr M, Goncalves P (2011) Behaviour of allanite during mylonitisation and implications for U–Th–Pb dating: case study at the Mt Mucrone, Italy. Lithos 125:40–50

Coggon R, Holland TJB (2002) Mixing properties of phengitic micas and revised garnet-phengite thermobarometers. J Metamorph Geol 20:683–696

Collins AS, Robertson AHF (1998) Processes of Late Cretaceous to Late Miocene episodic thrust-sheet translation in the Lycian Taurides, SW Turkey. J Geol Soc Lond 155:759–772

Copeland P, Parrish RR, Harrison TM (1983) Identification of inherited radiogenic Pb in monazite and its implications for U–b systematics. Lett Nat 333:760–763

Darling JR, Storey CD, Engi M (2012) Allanite U–Th–Pb geochronology by laser ablation ICPMS. Chem Geol 292–293:103–115

de Capitani C, Petrakakis K (2010) The computation of equilibrium assemblage diagrams with Theriak/Domino software. Am Mineral 95:1006–1016

Diener JFA, Powell R, White RW, Holland TJB (2007) A new thermodynamic model for clino- and orthoamphiboles in the system Na_2O– CaO–FeO–MgO–$Al2O_3$–SiO_2–H_2O–O. J Metamorph Geol 25:631–656

Dinter DA, Royden L (1993) Late Cenozoic extension in northeastern Greece: Strymon Valley detachment system and Rhodope metamorphic core complex. Geology 21:45–48

Gautier P, Brun J-P (1994) Crustalscale geometry and kinematics of lateorogenic extension in the central Aegean (Cyclades and Evvia Island). Tectonophysics 238:399–424

Gessner K, Ring U, Passchier CW, Güngör T (2001a) How to resist subduction: evidence for large-scale out-of-sequence thrusting during Eocene collision in western Turkey. J Geol Soc Lond 158:769–784

Gessner K, Ring U, Johnson C, Hetzel R, Passchier CW, Güngör T (2001b) An active bivergent rolling-hinge detachment system. Central Menderes metamorphic core complex in western Turkey. Geology 29:611–614

Gessner K, Collins A, Ring U, Güngör T (2004) Structural and thermal history of a poly-orogenic basement: U/Pb geochronology of granitoids rocks in southern Menderes Masif, Western Turkey. J Geol Soc Lond 16:101–193

Glodny J, Hetzel R (2007) Precise U–Pb ages of syn-extensional Miocene intrusions in the central Menderes Massif, western Turkey. Geol Mag 144(2):235–246

Gregory CJ, Rubatto D, Allen CM, Williams IS, Hermann J, Ireland T (2007) Allanite micro-geochronology: a LA-ICP-MS and SHRIMP U–Th–Pb study. Chem Geol 245:162–182

Gunther D, Heinrich CA (1999) Enhanced sensitivity in LA-ICPMS using helium–argon mixture as aerosol carrier. J Anal At Spectrom 14:1369–1374

Hetzel R, Reischmann T (1996) Intrusion age of Pan-African augen gneisses in the southern Menderes Massif and the age of cooling after Alpine ductile extensional deformation. Geol Mag 133(5):565–572

Hetzel R, Passchier CW, Ring U, Dora ÖO (1995) Bivergent extension in orogenic belts: the Menderes Massif (southwestern Turkey). Geology 23(5):455–458

Holland TJB, Powell R (1998) An internally consistent thermodynamic dataset for phases of petrological interest. J Metamorph Geol 16:309–343

Işık V, Tekeli O (2001) Late orogenic crustal extension in the northern Menderes Massif (western Turkey): evidences for metamorphic core complex formation. Int J Earth Sci 89:757–765

Isik V, Uysal T, Caglayan A, Seyitoglu G (2014) The evolution of intra-plate fault systems in central Turkey: structural evidence and Ar–Ar and Rb–Sr age constraints for the Savcili Fault Zone. Tectonics 33(10):1875–1899

Işık V, Seyitoğlu G, Cemen I (2003) Ductile-brittle transition along the Alaşehir shear zone and its structural relationship with the Simav detachment, Menderes Massif, western Turkey. Tectonophysics 374:1–18

Işık V, Tekeli O, Seyitoglu G (2004) The $^{40}Ar/^{39}Ar$ age of extensional ductile deformation and granitoid intrusions in the northern Menderes core complex: implications for the initiation of extensional tectonics in western Turkey. J Asian Earth Sci 23(4):555–566

Janots E, Engi M, Berger A, Allaz J, Schwarz J-O, Spandler C (2008) Prograde metamorphic sequence of REE minerals in pelitic rocks of the Central Alps: implications for allanite–monazite–xenotime phase relations from 250 to 610 °C. J Metamorph Geol 26(5):509–526

Jourdan F, Renne P (2007) Age calibration of the Fish Canyon sanidine $^{40}Ar/^{39}Ar$ dating standard using primary K–Ar standards. Geochim Cosmochim Acta 71:387–402

Kelsey DE, White RW, Powell R (2005) Calculated phase equilibria in K_2O–FeO–MgO–Al_2O_3–SiO_2–H_2O for silica-undersaturated sapphirine-bearing mineral assemblages. J Metamorph Geol 23:217–239

Koralay OE, Candan O, Chen F, Akal C, Oberhänsli R, Satir M, Dora OO (2012) Pan-African magmatism in the Menderes Massif: geochronological data from leucocratic tourmaline orthogneisses in western Turkey. Int J Earth Sci 101(8):2055–2081

Kröner A, Şengör AMC (1990) Archean and Proterozoic ancestry in late Precambrian to early Paleozoic crustal elements of southern Turkey as revealed by single-zircon dating. Geology 18:1186–1190

Lavier LL, Buck WR, Poliakov ANB (1999) Self-consistent rolling-hinge model for the evolution of large-offset, low-angle normal faults. Geology 27:1127–1130

Lister G, Banga G, Feenstra A (1984) Metamorphic core complexes of Cordilleran type in the Cyclades. Aegean Sea, Greece. Geology 12:221–225

Loos S, Reischmann T (1999) The evolution of the southern Menderes Massif in SW Turkey as revealed by zircon dating. J Geol Soc Lon 156:1021–1030

Ludwig KR (2003) Isoplot/Ex version 3.0. A geochronological toolkit for microsoft excel. Berkeley Geochronological Centre Special Publication, Berkeley, p 70

Malavieille J (2010) Impact of erosion, sedimentation, and structural heritage on the structure and kinematics of orogenic wedges: analog models and case studies. GSA Today 20:4–10

Miller EL, Gans PB, Garlin J (1983) The snake river décollement: an exhumed mid-tertiary brittle-ductile transition. Tectonics 2:239–263

Monié P, Torres-Toldán RL, García-Casco A (1994) Cooling and exhumation of the Western Betic Cordilleras $^{40}Ar/^{39}Ar$ thermochronological constraints on a collapsed terrane. Tectonophysics 228:353–379

Oberhänsli R, Candan O, Dora OO, Dürr S (1997) Eclogites within the Menderes Massif, western Turkey. Lithos 41:135–150

Oberhänsli R, Candan O, Wilke F (2010) Geochronological evidence of Pan-African eclogites from the cenral Menderes Massif, Turkey. Turk J Earth Sci 19:431–447

Okay AI (2001) Stratigraphic and metamorphic inversions in the central Menderes Massif: a new structural model. Int J Earth Sci 89:709–727

Okay IA, Satir M (2000) Coeval plutonism and metamorphism in a latest Oligocene metamorphic core complex in northwest Turkey. Geol Mag 137:495–516

Okay AI, Bozkurt E, Satır M, Yiğitbaş E, Crowley QG, Shang CK (2008) Defining the southern margin of Avalonia in the Pontides: geochronological data from the Late Proterozoic and Ordovician granitoids from NW Turkey. Tectonophysics 461:252–264

Özer S, Sözbilir H, Özkar I, Toker V, Sari B (2001) Stratigraphy of upper Cretaceous–Palaeocene sequences in the southern and eastern Menderes Massif. Int J Earth Sci 89:852–866

Poitrasson F, Chenery S, Shepperd TJ (2000) Electron microprobe and LA-ICP-MS study of monazite hydrothermal alteration: implications for U–Th–Pb geochronology and nuclear ceramics. Geochim Cosmochim Acta 64:3283–3297

Pourteau A, Candan O, Oberhänsli R (2009) High-pressure metasediments in central Turkey: constraints on the Neotethyan closure history. Tectonics. doi:10.1029/2009TC002650

Pourteau A, Sudo M, Candan O, Lanari P, Vidal O, Oberhänsli R (2013) Neotethys closure history of Anatolia: insight from ^{40}Ar–^{39}Ar geochronology and *P–T* estimation in high-pressure metasediments. J Metamorph Geol 31(6):585–606

Régnier JL, Ring U, Passchier CW, Gessner K, Güngör T (2003) Contrasting metamorphic evolution of metasedimentary rocks from the Cine and Selimiye nappes in the Anatolide belt, western Turkey. J Metamorph Geol 21:699–721

Rey PF, Teyssier C, Whitney DL (2009) Extension rates, crustal melting, and core complex dynamics. Geology 37:391–394

Rimmelé G, Oberhänsli R, Goffé B, Jolivet L, Candan O, Cetinkaplan M (2003) First evidence of high-pressure metamorphism in the 'Cover Series' of the southern Menderes Massif: tectonic and metamorphic implications for the evolution of SW Turkey. Lithos 71:19–46

Ring U, Gessner K, Gungor T, Passchier CW (1999) The Menderes Massif of western Turkey and the cycladic massif in the Aegean-do they really correlate? J Geol Soc Lond 156:3–6

Ring U, Johnson C, Hetzel R, Gessner K (2003) Tectonic denudation of a Late Cretaceous–Tertiary collisional belt: regionally symmetric cooling patterns and their relation to extensional faults in the Anatolide belt of western Turkey. Geol Mag 140:421–441

Satır M, Friedrichsen H (1986) The origin and evolution of the Menderes Massif, W-Turkey: a rubidium/strontium and oxygen isotope study. Geol Rundsch 75:703–715

Schenker FL, Gerya T, Burg J-P (2012) Bimodal behavior of extended continental lithosphere: modeling insight and application to thermal history of migmatitic core complexes. Tectonophysics 579:88–103

Sen Ş, Seyitoglu G (2009) Magnetostratigraphy of early–middle Miocene deposits from E–W trending Alaşehir and Büyük Menderes grabens in western Turkey, and its tectonic implications. In: van Hinsbergen DJJ, Edwards MA, Govers R (eds) Collision and collapse at the Africa–Arabia–Eurasia Subduction Zone. Geological Society of London Special Publication, London, pp 321–342

Seyitoglu G, Isik V, Cemen I (2004) Complete Tertiary exhumation history of the Menderes Massif, western Turkey: an alternative working hypothesis. Terra Nova 16(6):358–364

Seyitoglu G, Isik V, Esat K (2014) A 3D model for the formation of turtleback surfaces: the Horzum Turtleback of western Turkey as a case study. Turk J Earth Sci 23:479–494

Sherlock S, Kelley S, Inger S, Harris N, Okay A (1999) ^{40}Ar–^{39}Ar and Rb–Sr geochronology of high-pressure metamorphism and exhumation history of the Tavsanli Zone, NW Turkey. Contrib Mineral Petr 137(1):46–58

ten Veen JH, Boulton SJ, Alcicek MC (2009) From palaeotectonics to neotectonics in the Neotethys realm: the importance of kinematic decoupling and inherited structural grain in SW Anatolia (Turkey). Tectonophysics 437:261–281

Tera F, Wasserburg G (1972) U–Th–Pb systematics in three Apollo 14 basalts and the problem of initial Pb in lunar rocks. Earth Planet Sci Lett 14:281–304

Tirel C, Brun J-P, Burov E (2004) Thermomechanical modeling of extensional gneiss domes. In: Whitney DL, Teyssier C, Siddoway, CS (eds) Gneiss domes orogeny, vol 380. Geological Society of America papers, Boulder, Colorado, pp 67–78

Tirel C, Brun J-P, Burov E (2008) Dynamics and structural development of metamorphic core complexes. J Geophys Res 113:B04403. doi:10.1029/2005JB003694

Torsvik TH, Cocks LRM (2009) The lower paleozoic paleogeographical evolution of the northeastern and eastern peri-Gondwanan margin from Turkey to New Zealand. In: Bassett MG (ed) Geological society, vol 325. London Special Publications, London, pp 3–21

van Hinsbergen DJJ (2010) A key extensional metamorphic complex reviewed and restored: the Menderes Massif of western Turkey. Earth Sci Rev 102:60–76

Vandenberg LC, Lister GS (1996) Structural analysis of basement tectonites from the Aegean core complex of Ios, Cyclades, Greece. J Struct Geol 18:103–124

White RW, Powell R, Clarke GL (2002) The interpretation of reaction textures in Fe-rich metapelitic granulites of the Musgrave Block, central Australia: Constraints from mineral equilibria calculations in the system K_2O–FeO–MgO–Al_2O_3–SiO_2–H_2O–TiO_2–Fe_2O_3. J Metamorph Geol 20:41–55

White RW, Powell R, Holland TJB (2007) Progress relating to calculation of partial melting equilibria for metapelites. J Metamorph Geol 25(5):511

Whitney DL, Evans BW (2010) Abbreviations for names of rock-forming minerals. Am Mineral 95:185–187

Whitney DL, Teyssier C, Kruckenberg SC, Morgan VL, Iredale LJ (2008) High-pressure–low-temperature metamorphism of metasedimentary rocks, southern Menderes Massif, western Turkey. Lithos 101:218–232

Whitney DL, Teyssier C, Rey P, Buck WR (2013) Continental and oceanic core complexes. Geol Soc Am Bull. doi:10.1130/B30754.1

Wiedenbeck M, Hanchar JM, Peck WH, Sylvester P, Valley J, Whitehouse M, Kronz A, Morishita Y, Nasdala L, Fiebig J, Franchi I, Girard J-P, Greenwood RC, Hinton R, Kita N, Mason PRD, Norman M, Ogasawara M, Piccoli PM, Rhede D, Satoh H, Schulz-Dobrick B, Skår Ø, Spicuzza MJ, Terada K, Tindle A, Togashi S, Vennemann T, Xie Q, Zheng Y-F (2004) Further characterisation of the 91500 zircon crystal. Geostand Geoanal Res 28:9–39

Yılmaz Y, Genc SC, Gürer OF, Bozcu M, Yılmaz K, Karacık Z, Altunkaynak I, Elmas A (2000) When did the western Anatolian grabens begin to develop? In: Bozkurt E, Winchester JA, Piper JDA (eds) Tectonics and magmatism in Turkey and the surrounding area. Geological Society of London Special Publication, London, pp 353–384

Zeck HP, Monié P, Villa I, Hansen BT (1992) Very high rates of cooling and uplift in the Alpine Belt of the Betic Cordilleras, southern Spain. Geology 20:79–82